

Reconstruction algorithm for cross-waveband optical computing imaging

Jin-Tao Xie(谢锦涛), Shu-Hang Bie(别书航), Ming-Fei Li(李明飞), Yuan-Jin Yu(余远金), Yi-Fei Li(李毅飞), Jin-Guang Wang(王进光), Bao-Gang Quan(全保刚), and Ling-An Wu(吴令安)

Citation: Chin. Phys. B, 2024, 33 (**10**): 104203. DOI: 10.1088/1674-1056/ad6ccc
Journal homepage: http://cpb.iphy.ac.cn; http://iopscience.iop.org/cpb

What follows is a list of articles you may be interested in

High-quality ghost imaging based on undersampled natural-order Hadamard source

Kang Liu(刘炕), Cheng Zhou(周成), Jipeng Huang(黄继鹏), Hongwu Qin(秦宏伍), Xuan Liu(刘轩), Xinwei Li(李鑫伟), and Lijun Song(宋立军)

Chin. Phys. B, 2024, 33 (**9**): 094204. DOI: 10.1088/1674-1056/ad62e1

High-visibility ghost imaging with phase-controlled discrete classical light sources

Xueying Wu(仵雪滢), Yue Zhao(赵岳), and Liming Li(李利明)

Chin. Phys. B, 2024, 33 (**7**): 074202. DOI: 10.1088/1674-1056/ad4631

Efficient single-pixel imaging encrypted transmission based on 3D Arnold transformation

Zhen-Yu Liang(梁振宇), Chao-Jin Wang(王朝瑾), Yang-Yang Wang(王阳阳), Hao-Qi Gao(高皓琪), Dong-Tao Zhu(朱东涛), Hao-Li Xu(许颢砾), and Xing Yang(杨星)

Chin. Phys. B, 2024, 33 (**3**): 034204. DOI: 10.1088/1674-1056/acf204

Complex-amplitude Fourier single-pixel imaging via coherent structured illumination

Hong-Yun Hou(侯红云), Ya-Nan Zhao(赵亚楠), Jia-Cheng Han(韩佳成), De-Zhong Cao(曹 德忠),Su-Heng Zhang(张素恒), Hong-Chao Liu(刘宏超), and Bao-Lai Liang(梁宝来)

Chin. Phys. B, 2023, 32 (**6**): 064201. DOI: 10.1088/1674-1056/ac8e9a

Fast Fourier single-pixel imaging based on Sierra-Lite dithering algorithm

Zhen-Yu Liang(梁振宇), Zheng-Dong Cheng(程正东), Yan-Yan Liu(刘严严), Kuai-Kuai Yu(于快快), Yang-Di Hu(胡洋頔)

Chin. Phys. B, 2019, 28 (**6**): 064202. DOI: 10.1088/1674-1056/28/6/064202

Reconstruction algorithm for cross-waveband optical computing imaging

Jin-Tao Xie(谢锦涛)[1,2], Shu-Hang Bie(别书航)[1,2], Ming-Fei Li(李明飞)[1,2,†], Yuan-Jin Yu(余远金)[3], Yi-Fei Li(李毅飞)[1], Jin-Guang Wang(王进光)[1], Bao-Gang Quan(全保刚)[1,2], and Ling-An Wu(吴令安)[1,2,‡]

[1] *Institute of Physics, Chinese Academy of Sciences, Beijing* 100190, *China*
[2] *School of Physical Sciences, University of Chinese Academy of Sciences, Beijing* 100049, *China*
[3] *School of Automation, Beijing Institute of Technology, Beijing* 100081, *China*

(Received 30 June 2024; revised manuscript received 31 July 2024; accepted manuscript online 8 August 2024)

In a single-pixel fast imaging setup, the data collected by the single-pixel detector needs to be processed by a computer, but the speed of the latter will affect the image reconstruction time. Here we propose two kinds of setups which are able to transform non-visible into visible light imaging, wherein their computing process is replaced by a camera integration mode. The image captured by the camera has a low contrast, so here we present an algorithm that can realize a high quality image in near-infrared to visible cross-waveband imaging. The scheme is verified both by simulation and in actual experiments. The setups demonstrate the great potential for single-pixel imaging and high-speed cross-waveband imaging for future practical applications.

Keywords: optical computing imaging, single-pixel imaging

PACS: 42.30.–d **DOI:** 10.1088/1674-1056/ad6ccc

1. Introduction

In contrast to conventional optical imaging with two-dimensional (2D) multi-pixel detectors, single-pixel imaging (SPI) is a unique technique that reconstructs the image of an object with only a single-pixel detector through the second order correlation of a series of illumination spatial patterns and the corresponding total transmitted or reflected intensity from the object.[1] Because 2D detectors are no longer required, SPI may use high performance single-pixel detectors, which are difficult to manufacture in an array format.[2] For instance, photomultiplier tubes in SPI have been used for time-of-flight three-dimensional (3D) imaging,[3,4] single-photon imaging,[5] and non-line-of-sight imaging.[6] Ultrasonic transducers have been employed in SPI photoacoustic imaging.[7,8] The basic principle of SPI can be applied to electromagnetic waves of any wavelength, and even to particle imaging. Already, SPI has been realized throughout the spectrum from microwave[9] to terahertz[10,11] to hard x-rays[12–14] and even with atoms,[15] electrons,[16] and neutrons.[17,18] It has also been shown to have potential advantages in spatial resolution improvement,[19,20] radiation dose reduction,[14,21] and robustness in turbulence.[22]

For practical applications, SPI should have as good imaging quality and speed as conventional optical imaging. However, since every spatial pattern needs to be exposed, much more time is required to form an image compared to the single-shot exposure of conventional cameras. That is, SPI sacrifices imaging speed to eliminate the need for multiple pixels. A larger imaging field of view requires more modulation patterns, and consequently longer exposure times. The most common modulator in current use for SPI is the digital micromirror device (DMD), which is capable of reconfigurable displays of mega-pixel patterns at refresh rates of up to 32 kHz.[1] Since typical photodetectors can have bandwidths of MHz or even greater, the DMD refresh rate is the chief factor limiting the data acquisition rate. To overcome this, compressed sensing (CS) has been used to reduce the number of samples required,[23–25] but at the cost of more computing time for the process of iterative convex optimization.[23,25] Other alternatives to increase imaging speed include replacing the DMD with new light sources and modulators.[26–29] An array of 32×32 light-emitting diodes (LEDs) can switch patterns at a rate of 3.13 MHz and a CS-assisted 2D imaging rate of 2.5×10^4 frames per second (fps).[28,29] A rotating coded mask plate can project patterns at a rate of 2.4 MHz, which corresponds to a non-CS recovery of a 101×103 pixel size image at 72 fps.[27] Projection rates of up to 14.1 MHz and tunable frame sizes of up to 101×103 pixels have been realized using swept aggregate patterns that combine a DMD with laser scanning hardware.[30] In all the experiments above, the data processing power of the computer will affect the actual image reconstruction time. Recently, cross-waveband optical computing imaging replaced the computing process by camera integration.[31] By inputting the current of the near-infrared bucket signals from an object into the current driving an LED

†Corresponding author. E-mail: mf_li@iphy.ac.cn
‡Corresponding author. E-mail: wula@iphy.ac.cn

© 2024 Chinese Physical Society and IOP Publishing Ltd

and then reprojecting the emitted visible light onto the original modulation pattern, a visible spectrum image of the object was reconstructed directly with a high-dynamic-range camera.

Although the cross-waveband scheme has been experimentally demonstrated,[31] there is no satisfactory theoretical analysis, nor is there an appropriate algorithm to obtain an image with a high contrast from the low contrast image produced by the camera. In this paper, we analyze the imaging process in detail, provide an explanation for the cause of the low contrast, and provide algorithms for obtaining a high contrast image based on two popular measurement matrices. Our scheme is verified by both simulation and experiment, despite the low 8-bit or 16-bit readout mode of the camera. We also suggest a more suitable setup for practical applications with a translational or rotating scanning modulator, which allows a greater choice of light sources, while the cost may be much cheaper.

2. Theory and method

2.1. Imaging system design

We propose two kinds of setup which may be used in different circumstances, as shown in Fig. 1. In setup 1, light from the source is reflected off the object and then spatially modulated by a computational modulation device such as DMD1. After the total intensity of the modulated light field is collected by a bucket detector BD (also called a single-pixel detector) of suitable wavelength, the photoelectric signal is amplified to produce an output current for an LED. The visible light emitted from the LED is thus encoded with the object information, and is then directed onto a second DMD (DMD2). The camera is set to an appropriate exposure in synchrony with the modulation and decoding process to decode and obtain an image of the object. However, the image captured by the camera has a low contrast, which is the reason why we have analyzed the imaging process of this setup to find a way to improve image quality.

Setup 2 is a proposal for a system in which the source beam cannot be reflected by a DMD, or the object can only be measured in transmission mode. It also can be used with a visible light source for high-speed SPI[27] with cyclic modulation. In this setup, the emission source could be x-rays or even particles such as neutrons. As shown in the lower half of Fig. 1, after modulation by FM1 and projection onto an object, the total transmitted intensity is recorded by the bucket detector. The next process in the visible light arm is similar to that in setup 1, except that the beam undergoes a second modulation in FM2, which should be synchronized with FM1.

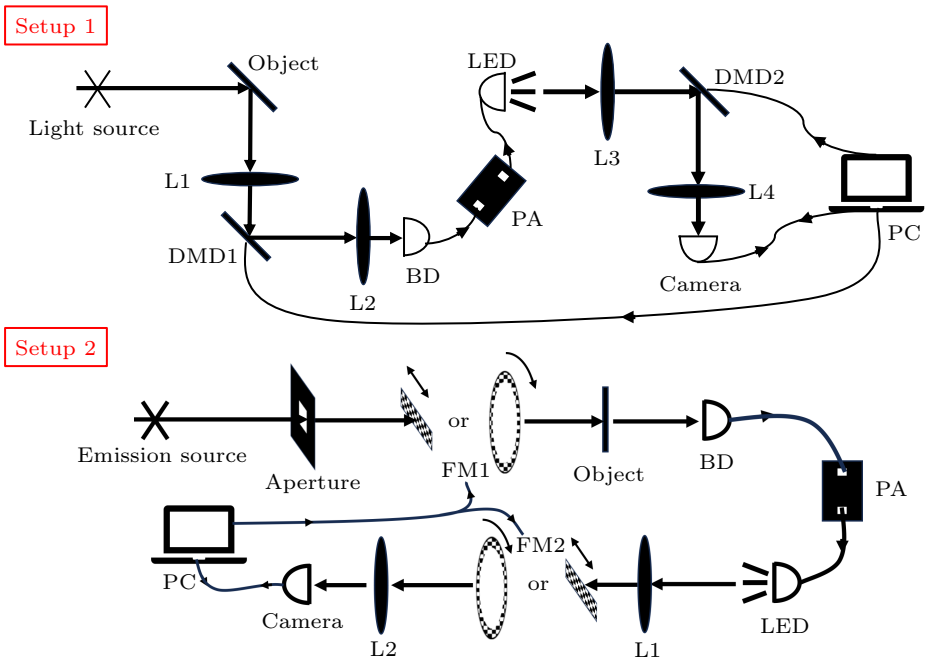


Fig. 1. Two setups for cross-waveband optical computing imaging. L1–L4: lenses, BD: bucket detector, PA: photoelectric amplifier, FM1 and FM2: fabricated masks in translational or rotating scanning mode, PC: computer.

2.2. Modulation pattern design

In theory, for full measurement in a normal single-pixel setup, it can be assumed that the modulation matrix is $\boldsymbol{A} = [\boldsymbol{a}_1, \ldots, \boldsymbol{a}_n]^{\mathrm{T}}$ and $\boldsymbol{a}_i, i = 1, \ldots, n$ is an n-element row vector while the object is an n-element column vector $\boldsymbol{x} = [x_1, \ldots, x_n]^{\mathrm{T}}$. The bucket signal's n-element column vector $\boldsymbol{b} = [b_1, \ldots, b_n]^{\mathrm{T}}$ can be expressed as

$$\boldsymbol{A}\boldsymbol{x} = \boldsymbol{b}, \tag{1}$$

where the element $b_i = \boldsymbol{a}_i \boldsymbol{x}$. Thus, we obtain the object information through the expression

$$\boldsymbol{x} = \boldsymbol{A}^{-1}\boldsymbol{b}, \tag{2}$$

where $\boldsymbol{A}^{-1}$ denotes the inverse of the matrix $\boldsymbol{A}$. In our setup, to realize cross-waveband imaging, we input the bucket signals of a given wavelength into the LED to create a visible light signal with the same intensity fluctuations as the bucket signals. The field reflected from DMD2 or fabricated mask FM2 can be treated as the bucket signal b_i multiplied by its modulation matrix $\boldsymbol{a}_i$. Thus, the n-element column vector $\boldsymbol{y} = [y_1, \ldots, y_n]^{\mathrm{T}}$ of the image captured by the camera with the same exposure time as that of one complete modulation process is

$$\boldsymbol{y} = \sum_{i=1}^{n} \boldsymbol{a}_i^{\mathrm{T}} b_i = \boldsymbol{A}^{\mathrm{T}} \boldsymbol{A} \boldsymbol{x}. \tag{3}$$

If we consider the noise component such as the readout noise as an n-element column vector $\boldsymbol{z} = [z_1, \ldots, z_n]^{\mathrm{T}}$, the form of the image can be changed to

$$\boldsymbol{y} = \sum_{i=1}^{n} \boldsymbol{a}_i^{\mathrm{T}} (b_i + z_i) = \boldsymbol{A}^{\mathrm{T}} (\boldsymbol{A}\boldsymbol{x} + \boldsymbol{z}). \tag{4}$$

Generally, the object and noise vectors are unknown while the modulation matrices can be designed manually. Thus, we next discuss the form of the image $\boldsymbol{y}$ based on different kinds of measurement matrices $\boldsymbol{A}$.

2.2.1. Hadamard matrices

The Hadamard matrix is well known and frequently used in SPI because of its complete and orthogonal basis. The common form of the matrix is

$$\boldsymbol{H}_{2n} = \begin{bmatrix} \boldsymbol{H}_n & \boldsymbol{H}_n \\ \boldsymbol{H}_n & -\boldsymbol{H}_n \end{bmatrix}, \tag{5}$$

where $\boldsymbol{H}_1 = [1]$ and $n = 2^i$, $i \in N^+$. However, in reality, the value of the element cannot be -1, so we replace the -1's with 0's, and denote the matrix as $\boldsymbol{H}_n^Z$. It still retains symmetry ($\boldsymbol{H}_n^Z = \boldsymbol{H}_n^{Z^{\mathrm{T}}}$), so after performing self-correlation we obtain

$$\boldsymbol{H}_n^{Z^{\mathrm{T}}} \boldsymbol{H}_n^Z = \frac{n}{4}(\boldsymbol{J} + \boldsymbol{I} + \boldsymbol{J}_{1,:} + \boldsymbol{J}_{:,1}), \tag{6}$$

where $\boldsymbol{J}$ and $\boldsymbol{I}$ denote the all-ones matrix and the identity matrix of size $n \times n$, respectively; $\boldsymbol{J}_{1,:}$ and $\boldsymbol{J}_{:,1}$ are $n \times n$ matrices with all-zero elements except for an all-ones first row and an all-ones first column, respectively. If we use this Hadamard matrix as our measurement matrix, we can calculate the image as

$$\boldsymbol{y} = \boldsymbol{H}_n^{Z^{\mathrm{T}}} \boldsymbol{H}_n^Z \boldsymbol{x} = \frac{n}{4} \left(\boldsymbol{x}_{\mathrm{sum}} + \boldsymbol{x} + \begin{bmatrix} \|\boldsymbol{x}\| \\ 0 \\ \vdots \\ 0 \end{bmatrix} + \begin{bmatrix} \boldsymbol{x}1 \\ \vdots \\ \boldsymbol{x}1 \end{bmatrix} \right), \tag{7}$$

where $\boldsymbol{x}_{\mathrm{sum}} = [\|\boldsymbol{x}\|, \ldots, \|\boldsymbol{x}\|]^{\mathrm{T}}$ of size $n \times 1$, $\boldsymbol{x}$ is the object's n-element column vector, and $\|\boldsymbol{x}\|$ denotes the sum of all elements in the $\boldsymbol{x}$ vector. Because all the elements of the first row and first column of the measurement matrix $\boldsymbol{H}_n^Z$ are 1, the first pixel of the image will have the largest gray scale value, i.e., pure white, as we can see from Eq. (7), which will result in a low overall contrast. Thus, we may eliminate the first row and first column of $\boldsymbol{H}_n^Z$ to obtain $\boldsymbol{H}_{n-1}^R$, which is called the reduced Hadamard matrix.[32]

2.2.2. Reduced Hadamard matrices

To apply the reduced Hadamard matrix in our setup, we first calculate its self-correlation form

$$\boldsymbol{H}_{n-1}^{R^{\mathrm{T}}} \boldsymbol{H}_{n-1}^R = \frac{n-4}{4} \left(\boldsymbol{J}_{n-1} + \frac{n}{n-4} \boldsymbol{E}_{n-1} \right). \tag{8}$$

Then, we can obtain the image as

$$\boldsymbol{y}^R = \boldsymbol{H}_{n-1}^{R^{\mathrm{T}}} \boldsymbol{H}_{n-1}^R x = \frac{n-4}{4} \left(\boldsymbol{x}_{\mathrm{sum}} + \frac{n}{n-4} \boldsymbol{x} \right), \tag{9}$$

where $\boldsymbol{x}$ is the object's column vector that consists of $(n-1)$ elements. In our setup, the image captured by the camera is the $\boldsymbol{y}^R$ vector, and we can calculate its contrast theoretically as

$$\begin{aligned} y_{\mathrm{contrast}}^R &= \frac{\boldsymbol{y}^R.\max - \boldsymbol{y}^R.\min}{\boldsymbol{y}^R.\max + \boldsymbol{y}^R.\min} \\ &= \frac{\boldsymbol{x}.\max - \boldsymbol{x}.\min}{\boldsymbol{x}.\max + \boldsymbol{x}.\min + (2 - \frac{8}{n})\|\boldsymbol{x}\|} < x_{\mathrm{contrast}}, \end{aligned} \tag{10}$$

where $\{\}.\max$ and $\{\}.\min$ are the maximum and minimum values of the matrix or vector, respectively. With the increase of the pixel number n, the contrast of the image will decrease slightly and ultimately approach a constant value. Since the contrast is low because $\|\boldsymbol{x}\|$ is very large, we need to figure out how to recover a better image from the low contrast image captured by the camera. Based on Eq. (9), we can deduce the object vector as

$$\boldsymbol{x} = \frac{4}{n} \boldsymbol{y}^R - \frac{n-4}{n} \boldsymbol{x}_{\mathrm{sum}}. \tag{11}$$

Although we cannot obtain $\boldsymbol{x}$ from an unknown $\boldsymbol{x}_{\mathrm{sum}}$, fortunately, it can be expressed in terms of $\boldsymbol{y}_{\mathrm{sum}}^R$ as

$$\boldsymbol{x}_{\mathrm{sum}} = \frac{4}{(n-2)^2} \boldsymbol{y}_{\mathrm{sum}}^R, \tag{12}$$

where $\boldsymbol{y}_{\mathrm{sum}}^R = [\|\boldsymbol{y}^R\|, \ldots, \|\boldsymbol{y}^R\|]^{\mathrm{T}}$. Thus, the object vector is

$$\boldsymbol{x} = \frac{4}{n} \left(\boldsymbol{y}^R - \frac{n-4}{(n-2)^2} \boldsymbol{y}_{\mathrm{sum}}^R \right). \tag{13}$$

Considering the noise $\boldsymbol{z} = [z_1, \ldots, z_{n-1}]^{\mathrm{T}}$ in the imaging process, the image and the object can be expressed as

$$\begin{aligned} \boldsymbol{y}^R &= \boldsymbol{H}_{n-1}^{R^{\mathrm{T}}} (\boldsymbol{H}_{n-1}^R \boldsymbol{x} + \boldsymbol{z}) \\ &= \frac{n-4}{4} \left(\boldsymbol{x}_{\mathrm{sum}} + \frac{n}{n-4} \boldsymbol{x} \right) + \boldsymbol{H}_{n-1}^{R^{\mathrm{T}}} \boldsymbol{z}, \end{aligned} \tag{14}$$

$$\boldsymbol{x} = \frac{4}{n} \left(\boldsymbol{y}^R - \frac{n-4}{(n-2)^2} \boldsymbol{y}_{\mathrm{sum}}^R - \boldsymbol{H}_{n-1}^{R^{\mathrm{T}}} \boldsymbol{z} \right). \tag{15}$$

In the case that the noise is constant, the values of all the elements in $\boldsymbol{H}_{n-1}^{R^{\mathrm{T}}}\boldsymbol{z}$ are the same. Thus, the image captured by the camera contains the information of the object superposed on a large uniform gray scale background, which means that we can choose an appropriate background value as the noise and subtract it from the image vector $\boldsymbol{y}^R$ to recover a higher contrast image. This was performed using the python program shown in the Data availability section below. The specific process can be described as follows. For a typical 8-bit low contrast image, we first split the gray values of the pixels into 255 parts, each part having a gray value range of 1, e.g., 0–1, 1–2, ... Then we sum the number of the pixels in each part, and take the gray value with the highest number of pixels as the background value to be subtracted.

2.2.3. Cyclic *S*-matrices

In contrast to the above Hadamard matrices, the cyclic *S*-matrix has advantages in high-speed SPI because its row is the cyclic left shift of the previous row.[30] There are three methods to construct cyclic *S*-matrices,[33] but here we only discuss the twin prime construction. This scheme produces a cyclic *S*-matrix $\boldsymbol{S}$ of order n whenever $n = p(p+2)$ and both p and $p+2$ are prime numbers. Let $S_{i,j}$ denote the element of $\boldsymbol{S}$ with row index i and column index j. The initial row $S_{0,j}$ $(j = 0,\ldots,n-1)$ determines all elements of $\boldsymbol{S}$ according to

$$S_{i,j} = \begin{cases} S_{0,i+j}, & \text{if} \quad i+j < n, \\ S_{0,i+j-n}, & \text{if} \quad i+j \geq n, \end{cases} \tag{16}$$

where $i = 0,\ldots,n-1$.

An integer x is regarded as a quadratic residue (mod y) if $x \neq 0$ (mod y) and there exists another integer z such that $x \equiv z^2$ (mod y). In this case, suppose p and $q = p+2$ are both prime numbers such as $p = 3$, $q = 5$, then we can define

$$f(j) = \begin{cases} +1, & \text{if } j \text{ is a quadratic residue (mod } p), \\ 0, & \text{if } j \equiv 0 \text{ (mod } p), \\ -1, & \text{otherwise}, \end{cases} \tag{17}$$

$$g(j) = \begin{cases} +1, & \text{if } j \text{ is a quadratic residue (mod } q), \\ 0, & \text{if } j \equiv 0 \text{ (mod } q), \\ -1, & \text{otherwise}, \end{cases} \tag{18}$$

$$S_{0,j} = \begin{cases} 0, & \text{if} \quad [f(j)-g(j)]g(j) = 0, \\ +1, & \text{otherwise}. \end{cases} \tag{19}$$

To apply the cyclic *S*-matrix to our setup, we first calculate the self-correlation as

$$\boldsymbol{S}^{\mathrm{T}}\boldsymbol{S} = \frac{n+1}{4}(\boldsymbol{J}+\boldsymbol{I}), \tag{20}$$

where $n = p \times q$, and $\boldsymbol{J}$ and $\boldsymbol{I}$ denote the all-ones matrix and the identity matrix of size $n \times n$, respectively. Based on this, we can obtain the image captured by the camera as

$$\boldsymbol{y}^{\boldsymbol{S}} = \boldsymbol{S}^{\mathrm{T}}\boldsymbol{S}\boldsymbol{x} = \frac{n+1}{4}(\boldsymbol{x}_{\mathrm{sum}} + \boldsymbol{x}). \tag{21}$$

The theoretical contrast of $\boldsymbol{y}^{\boldsymbol{S}}$ is

$$\begin{aligned} y_{\mathrm{contrast}}^{\boldsymbol{S}} &= \frac{\boldsymbol{x}.\max - \boldsymbol{x}.\min}{\boldsymbol{x}.\max + \boldsymbol{x}.\min + 2\|\boldsymbol{x}\|} \\ &= \lim_{n\to+\infty} y_{\mathrm{contrast}}^{R} < y_{\mathrm{contrast}}^{R}. \end{aligned} \tag{22}$$

From Eqs. (10) and (22) we can see that the reduced Hadamard matrix may have a slight advantage in having a higher contrast compared with the cyclic *S*-matrix, but that disappears gradually when the number of pixels n increases.

To recover a high contrast image, we deduce the object vector from Eq. (21) to be

$$\boldsymbol{x} = \frac{4}{n+1}\left(\boldsymbol{y}^{\boldsymbol{S}} - \frac{1}{n+1}\boldsymbol{y}_{\mathrm{sum}}^{\boldsymbol{S}}\right), \tag{23}$$

where

$$\boldsymbol{y}_{\mathrm{sum}}^{\boldsymbol{S}} = \frac{(n+1)^2}{4}\boldsymbol{x}_{\mathrm{sum}}.$$

When we include the noise $\boldsymbol{z} = [z_1,\ldots,z_n]^{\mathrm{T}}$, the image and the object become, respectively,

$$\boldsymbol{y}^{\boldsymbol{S}} = \boldsymbol{S}^{\mathrm{T}}(\boldsymbol{S}\boldsymbol{x}+\boldsymbol{z}) = \frac{n+1}{4}(\boldsymbol{x}_{\mathrm{sum}}+\boldsymbol{x}) + \boldsymbol{S}^{\mathrm{T}}\boldsymbol{z}, \tag{24}$$

$$\boldsymbol{x} = \frac{4}{n+1}\left(\boldsymbol{y}^{\boldsymbol{S}} - \frac{1}{n+1}\boldsymbol{y}_{\mathrm{sum}}^{\boldsymbol{S}} - \boldsymbol{S}^{\mathrm{T}}\boldsymbol{z}\right). \tag{25}$$

The high-contrast imaging retrieval process for the cyclic *S*-matrix is the same as that for the reduced Hadamard matrix because their low-contrast images both contain the information of the object superposed on a large uniform gray scale background.

2.2.4. Reduced Hadamard matrices *versus* cyclic *S*-matrices

In the analysis above, we know the reduced Hadamard matrix has a slightly higher contrast than the cyclic *S*-matrix for the same number of imaging pixels. However, this does not necessarily mean that it is better in all aspects. Figures 2(a1), 2(a2) and 2(b1), 2(b2) show two 15×15 reduced Hadamard and cyclic *S*-matrices and their patterns reshaped by each row, respectively. For the former, the reshaped dissimilar patterns are directly combined in Fig. 2(a3) to create a translation scanning mask. For the latter, adjacent patterns are very similar, and only the last column of the matrix is different, as can be seen by comparing the green and red rectangles in Fig. 2(b2). Thus, we can combine these patterns to a very small size, and every time we move a pixel we can acquire a new pattern, as shown in Fig. 2(b3). Therefore, for a setup 2 mask the cyclic *S*-matrix is more suitable when high-speed SPI is required.

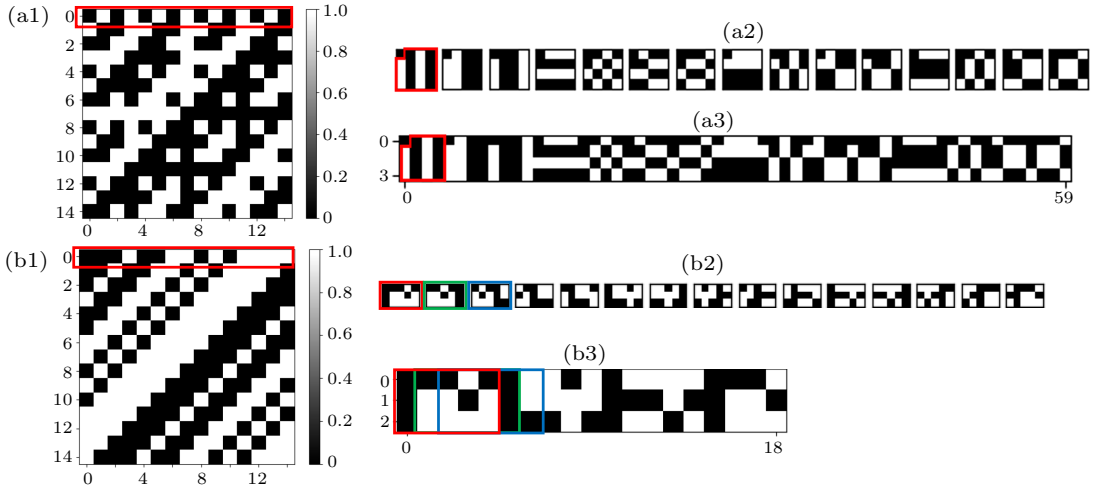


Fig. 2. Two 15×15 pattern designs for (a1) a reduced Hadamard matrix and (b1) a cyclic *S*-matrix. (a2) and (b2) The reshaped patterns from each row in panels (a1) and (b1), respectively. (a3) and (b3) Recombination of all the patterns in panels (a2) and (b2), respectively.

3. Simulation and experimental results

To verify the efficacy of our proposed algorithm, we first simulate imaging of the binary image number '5' based on our setup with different kinds of measurement matrices. The measurement matrices of the three columns from left to right in Fig. 3 are the Hadamard, reduced Hadamard, and cyclic *S*-matrices, respectively. Figures 3(a1)–3(a3) show the bucket signals of one complete modulation process; note the different values of the axes. The fluctuations in Figs. 3(a2) and 3(a3) will be reproduced by the emitted light field intensities of LED and recorded by the camera's integration mode to obtain the full information of the object. Figures 3(b1)–3(b3) are the images reconstructed using the accumulated intensities based on Eqs. (7), (9), and (21); here the color bar ranges were automatically chosen by the simulation program, and the maximum and minimum gray values of the background and the object are 84900–42400, 42586–42330, and 37575–37350, respectively. Because of the default color bar of the program, the images of the accumulated intensities of both Figs. 3(b2) and 3(b3) look the same as their original input images. However, in an actual experiment, the gray scale depends on the number of bits read out by the camera, and so we manually set an 8-bit readout in the program. The images are depicted in Figs. 3(c1)–3(c3), where in Fig. 3(c1) we can see that the object's information is completely obscured by the background because of the pure white first pixel in the figure, while in Figs. 3(c2)–3(c3) the images have a very low contrast and are barely visible. The values of the contrast agree with those calculated from Eqs. (10) and (22). By applying Eqs. (13) and (23), we can obtain two images with a high contrast from Figs. 3(c2)–3(c3), as shown in Figs. 3(d2)–3(d3).

Next, we conduct a real imaging experiment based on setup 1. The light source is a near-infrared lamp. The object is a letter 'B' made out of plastic. The DMD1 (DLP9500) and DMD2 (ViALUXV-7001) are programmed with the same series of $(32 \times 32) - 1$ reduced Hadamard patterns. The beam reflected from DMD1 is collected by a near-infrared single-pixel detector BD (HS-PD1000-2). The camera is a high-dynamic-range CCD camera (ASI2600MC) with 8-bit and 16-bit readout modes. The effective imaging size of the camera is 768×1360 pixels. The setup mentioned above is similar to that in Ref. [31], but the DMDs's frequency was set to 1 kHz and the two integration times of the camera were 1.023 s. The images read out by the camera in the 8-bit and 16-bit modes are shown in Figs. 4(a1) and 4(b1), respectively, where the gray diamonds are the imaging field of view. It can be seen that the gray background of the image in the second figure is brighter than in the first, but neither of the object signals is distinguishable. Based on Eq. (15), we can recover two high contrast images by processing the above images, as shown in Figs. 4(a2) and 4(b2). To figure out the reason for the different backgrounds of the 8-bit and 16-bit modes, we first proportionally compress the grayscale of the 16-bit readout to 8-bit and make sure it is an integer from 0 to 255. Then we plot the gray values along the marked red, yellow, blue, and green cross sections of Figs. 4(a1)–4(b1) versus pixel positions, as shown in Fig. 4(c). We can see that the gray values of the green line in the compressed 16-bit image are higher than those of the yellow line in the 8-bit image, which is why the former has a brighter background. On the other hand, we find that the red solid line of the latter is lower than the blue solid line, i.e., the 8-bit image has a lower minimum gray value compared with the 16-bit case, which has a denoising effect on the image. Though both readout modes can retrieve images with a good contrast, the 16-bit readout can have a better intensity resolution, which is important for distinguishing the small bucket signal fluctuations as shown in Figs. 3(a2)–3(a3).

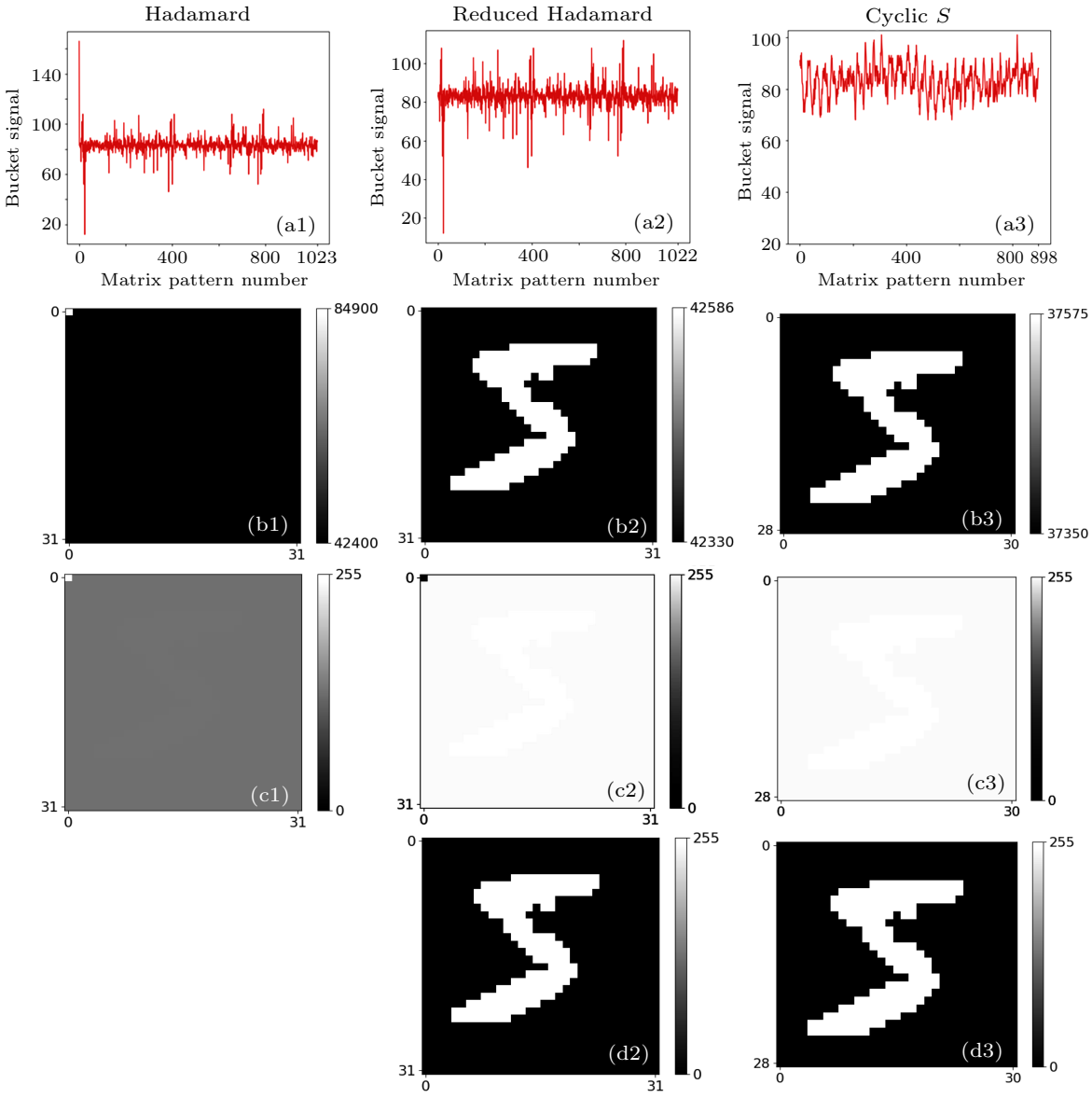


Fig. 3. Simulation results. (a1)–(a3) Bucket signals versus measurement frame number for the Hadamard, reduced Hadamard, and cyclic *S*-matrices, respectively. (b1)–(b3) Images obtained from accumulated intensities without manually setting the color bar range; note the different maximum values 84900, 43586, and 37575 of the color bars. (c1)–(c3) Proportional compression of the gray scale in panels (b1)–(b3) with a unified color bar from 0–255 (assuming an 8-bit readout camera). (d2)–(d3) Images reconstructed from panels (c2)–(c3) by using our proposed algorithm.

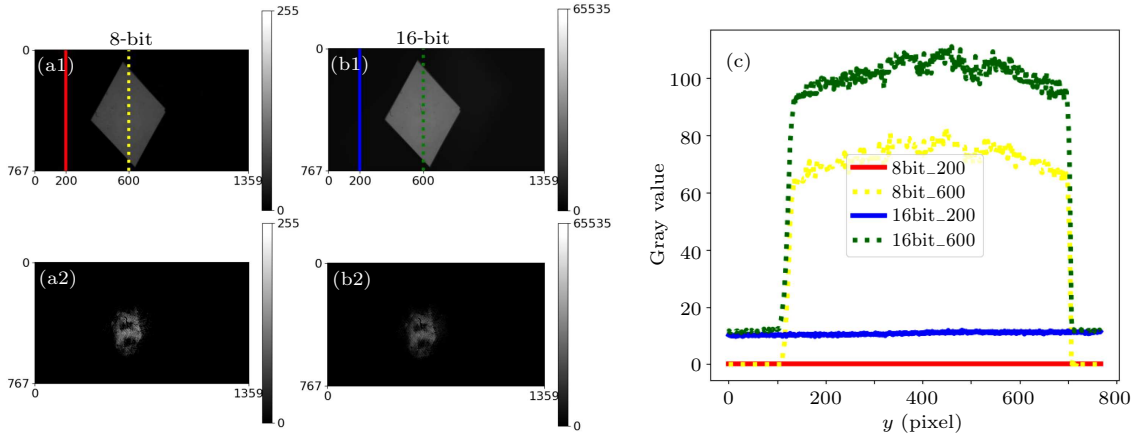


Fig. 4. Experimental results. (a1) and (b1) Images captured by the camera in 8-bit and 16-bit readout modes, respectively. (a2) and (b2) Images recovered by our new algorithm. (c) Rescaled gray scale of the images versus the *y* axis pixel number from panels (a1)–(b1) for the 8-bit (red solid and yellow dotted lines) and 16-bit readout modes (blue solid and green dotted lines). The color bars are automatically generated by the camera and do not reflect the actual gray values.

4. Conclusion

In conclusion, we have proposed an algorithm for retrieving an image with a high contrast from the low contrast image captured by the camera in cross-waveband optical computing imaging. We choose a binary image number '5' as an object and simulate its reconstruction with the Hadamard, reduced Hadamard and cyclic *S*-modulation matrices. The first is not suitable because of the presence of the highest gray tone in the first pixel of the image captured by the camera. The reduced Hadamard matrix has a slightly higher contrast than the cyclic *S*-matrix for the same number of imaging pixels, and both two matrices can be used in setup 1. For more practical applications, we propose setup 2 with a translational or rotating scanning modulator, where we have a wider choice of light sources and the cost may be much cheaper. The cyclic *S*-matrix has a considerable advantage in the fabrication of its mask plate because of the similarity of its patterns, and is the most suitable matrix for setup 2. We have successfully retrieved high contrast images by our method through simulation with a reduced Hadamard matrix and cyclic *S*-matrix, as well as in real experiments (from near-infrared to visible) with a $(32 \times 32) - 1$ reduced Hadamard matrix for both 8-bit and 16-bit readout modes of the camera. We believe our work may be of great benefit to cross-waveband optical computing imaging in various future practical applications.

Data availability statement

Data underlying the results and the algorithm codes are available in https://github.com/NoobJintao/cross-waveband-optical-computing-imaging.

References

[1] Edgar M P, Gibson G M and Padgett M J 2019 *Nat. Photon.* **13** 13
[2] Sun M J and Zhang J M 2019 *Sensors* **19** 732
[3] Gong W, Zhao C, Yu H, Chen M, Xu W and Han S 2016 *Sci. Rep.* **6** 26133
[4] Sun M J, Edgar M P, Gibson G M, Sun B, Radwell N, Lamb R and Padgett M J 2016 *Nat. Commun.* **7** 12010
[5] Zhao W, Chen H, Yuan Y, Zheng H, Liu J, Xu Z and Zhou Y 2019 *Phys. Rev. Appl.* **12** 034049
[6] Chen Q, Chamoli S K, Yin P, Wang X and Xu X 2018 *Laser Phys. Lett.* **15** 126201
[7] Liang J, Gao L, Li C and Wang L V 2014 *Opt. Lett.* **39** 430
[8] Torke P R, Nuster R and Paltauf G 2022 *Opt. Lett.* **47** 1462
[9] Diebold A V, Imani M F, Sleasman T and Smith D R 2018 *Optica* **5** 1529
[10] Olivieri L, Gongora J S T, Pasquazi A and Peccianti M 2018 *ACS Photon.* **5** 3379
[11] Watts C M, Shrekenhamer D, Montoya J, Lipworth G, Hunt J, Sleasman T, Krishna S, Smith D R and Padilla W J 2014 *Nat. Photon.* **8** 605
[12] Pelliccia D, Rack A, Scheel M, Cantelli V and Paganin D M 2016 *Phys. Rev. Lett.* **117** 113902
[13] Yu H, Lu R, Han S, Xie H, Du G, Xiao T and Zhu D 2016 *Phys. Rev. Lett.* **117** 113901
[14] Zhang A X, He Y H, Wu L A, Chen L M and Wang B B 2018 *Optica* **5** 374
[15] Khakimov R I, Henson B M, Shin D K, Hodgman S S, Dall R G, Baldwin K G H and Truscott A G 2016 *Nature* **540** 100
[16] Li S, Cropp F, Kabra K, Lane T J, Wetzstein G, Musumeci P and Ratner D 2018 *Phys. Rev. Lett.* **121** 114801
[17] Kingston A M, Myers G R, Pelliccia D, Salvemini F, Bevitt J J, Garbe U and Paganin D M 2020 *Phys. Rev. A* **101** 053844
[18] He Y H, Huang Y Y, Zeng Z R, Li Y F, Tan J H, Chen L M, Wu L A, Li M F, Quan B G, Wang S L and Liang T J 2021 *Sci. Bull.* **66** 133
[19] Oh J E, Cho Y W, Scarcelli G and Kim Y H 2013 *Opt. Lett.* **38** 682
[20] He Y H, Zhang A X, Li M F, Huang Y Y, Quan B G, Li D Z, Wu L A and Chen L M 2020 *APL Photon.* **5** 056102
[21] Lane T J and Ratner D 2020 *Opt. Express* **28** 5898
[22] Cheng J 2009 *Opt. Express* **17** 7916
[23] Takhar D, Laska J N, Wakin M B, Duarte M E, Baron D, Sarvotham S, Kelly K E and Baraniuk R G 2006 *Proc. SPIE* **6065** 606509
[24] Vaz P G, Amaral D, Requicha Ferreira L F, Morgado M and Cardoso J 2020 *Opt. Express* **28** 11666
[25] Jiang W, Li X, Peng X and Sun B 2020 *Opt. Express* **28** 7889
[26] Kanno H, Mikami H and Goda K 2020 *Opt. Lett.* **45** 2339
[27] Hahamovich E, Monin S, Hazan Y and Rosenthal A 2021 *Nat. Commun.* **12** 4516
[28] Xu Z H, Chen W, Penuelas J, Padgett M and Sun M J 2018 *Opt. Express* **26** 2427
[29] Huang H, Li L, Ma Y and Sun M 2022 *Electron. Mater.* **3** 93
[30] Kilcullen P, Ozaki T and Liang J 2022 *Nat. Commun.* **13** 7879
[31] Bie S H, Xie J T, Zhang Y X, Li M F, Yu W K and Chen X H 2024 *Opt. Lett.* **49** 2413
[32] Wang G, Zheng H, Tang Z, Zhou Y, Chen H, Liu J, He Y, Yuan Y, Li F and Xu Z 2020 *Sci. Rep.* **10** 2493
[33] Harwit M and Sloane N J A 1979 *Hadamard transform optics* (Elsevier)